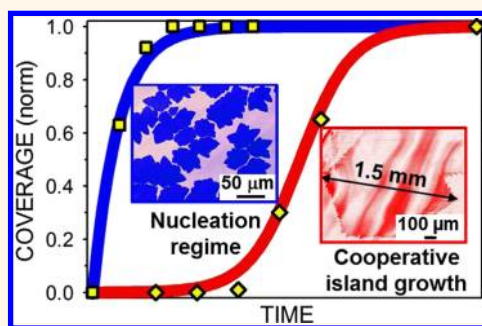


# Cooperative Island Growth of Large-Area Single-Crystal Graphene on Copper Using Chemical Vapor Deposition

Gyula Eres,<sup>†,\*</sup> Murari Regmi,<sup>†</sup> Christopher M. Rouleau,<sup>‡</sup> Jihua Chen,<sup>‡</sup> Ilia N. Ivanov,<sup>‡</sup> Alexander A. Puretzky,<sup>‡</sup> and David B. Geohegan<sup>‡</sup>

<sup>†</sup>Materials Science and Technology Division, and <sup>‡</sup>Center for Nanophase Materials Sciences, Oak Ridge National Laboratory, Oak Ridge, Tennessee 37831, United States

**ABSTRACT** In this work we explore the kinetics of single-crystal graphene growth as a function of nucleation density. In addition to the standard methods for suppressing nucleation of graphene by pretreatment of Cu foils using oxidation, annealing, and reduction of the Cu foils prior to growth, we introduce a new method that further reduces the graphene nucleation density by interacting directly with the growth process at the onset of nucleation. The successive application of these two methods results in roughly 3 orders of magnitude reduction in graphene nucleation density. We use a kinetic model to show that at vanishingly low nucleation densities carbon incorporation occurs by a cooperative island growth mechanism that favors the formation of substrate-size single-crystal graphene. The model reveals that the cooperative growth of millimeter-size single-crystal graphene grains occurs by roughly 3 orders of magnitude increase in the reactive sticking probability of methane compared to that in random island nucleation.



**KEYWORDS:** graphene · chemical vapor deposition · growth kinetics · nucleation density · cooperative island growth

Direct growth of graphene on various surfaces is the most promising approach for controlling the synthesis of large-area single-crystal sheets needed for various technological applications. Chemical vapor deposition (CVD) on Cu foils using  $\text{CH}_4$  performed either at low pressure<sup>1–4</sup> (LPCVD) or atmospheric pressure<sup>5–10</sup> (APCVD) emerged as the simplest and most promising method for implementing graphene growth by a surface-limited process. The possibility of scaling up graphene growth by  $\text{CH}_4$  CVD has been explored using a roll-to-roll apparatus utilizing Cu foils of up to 30 in. wide.<sup>11</sup> Although uniform coverage has been demonstrated, the graphene grown in this process consists of a mixture of single-layer (SL) and multilayer (ML) domains patched together into an extended quilt. The imperfect alignment of these small patches is compensated by formation of grain boundaries<sup>12–15</sup> consisting of pentagon–heptagon pair defect networks.<sup>4,13,16,17</sup> The high density of grain boundaries and defects must be reduced or

entirely eliminated because they impede carrier transport<sup>18,19</sup> by intervalley scattering,<sup>7,20</sup> mechanically weaken the graphene,<sup>13,21</sup> and promote undesirable surface reactions with adsorbates from the environment.<sup>14</sup> In contrast, a steady increase of the size of the graphene single crystals has been achieved by optimizing CVD growth in research-scale processes. A few hundred micrometer flakes of single-crystal graphene are now routinely grown, with the lateral size reaching 1 cm in a recent report.<sup>22–30</sup>

While the focus in these synthesis processes is on increasing the size of the single-crystal grains (SCGs), the current approaches are limited to trial and error because of the lack of understanding of the reaction steps governing nucleation and growth. The typical parameters include the growth temperature, reactor pressure, the growth gas composition, and Cu foil pretreatment. The main achievement of this approach is the recognition that the size of single crystal graphene patches is related

\* Address correspondence to eresg@ornl.gov.

Received for review January 13, 2014 and accepted May 15, 2014.

Published online May 15, 2014  
10.1021/nn500209d

© 2014 American Chemical Society

inversely to the nucleation density. Hypothetically, the entire substrate could be covered with a single grain starting from one nucleation site growing without interference from any other nucleation site, analogous to screw dislocation-driven crystal growth. The growth conditions for realizing such a process require suppressing the nucleation density while simultaneously promoting the lateral growth rate of graphene, creating special kinetics that has not been explored previously.

In this work, we focus on understanding the role that the nucleation density of graphene on Cu foils, defined as the number of nucleation sites per unit area, plays in determining the graphene growth mode. We apply concepts from classical nucleation theory, originally developed for thin film growth processes, to illustrate the important steps in graphene growth.<sup>31</sup> From the perspective of promoting large-area graphene growth, the nucleation density determines the largest island size that can be obtained before coalescence causes two or more individual islands to merge into successively larger islands. In epitaxial thin film growth, coalescence can disrupt long-range order and lead to lattice imperfections that are undesirable in large-area single-crystal graphene growth. Here, we describe a two-step approach for controlling the nucleation stage that includes reducing the nucleation site density followed by a second step to suppress nucleation at the remaining nucleation sites. Note that these two factors are interrelated and cannot always be uncoupled and treated separately. To reduce the nucleation density, we first use intentional oxidation of the Cu foils in air prior to graphene growth. The role of this step is to remove surface impurities such as carbon contamination and other metallic impurities by oxidation. In addition, the number of structural defects on the surface is dramatically reduced by regrowth of Cu grains after reduction during the H<sub>2</sub> annealing step that precedes graphene growth. We also report collisional deactivation (CD) for the first time as a method to suppress nucleation at the remaining nucleation sites after the oxidation/reduction step. The role of CD is to effectively increase the reaction barrier for nucleation by removing enough energy from activated precursors to bring a fraction of activated carbon species below the threshold.<sup>32</sup> In practice, we perform CD by transient cooling using a brief, 10 s duration pulse of Ar at the onset of graphene growth. The use of collisions with inert gas atoms is a familiar approach for changing the rate and the outcome of unimolecular thermal decomposition reactions of hydrocarbons.<sup>33,34</sup> Combining these two steps in succession to suppress nucleation in graphene CVD on Cu foils, we demonstrated the growth of large SL SCGs of up to 1.5 mm in lateral size. We use a kinetic model to show that in the extreme limits of nucleation density graphene growth occurs by distinctly different growth mechanisms. At high nucleation densities graphene growth occurs by

coalescence of individual islands, which results in grain boundary formation. In contrast, carbon incorporation at vanishing nucleation densities occurs by a cooperative island growth mode that intrinsically produces large-area single-crystal graphene.

## RESULTS AND DISCUSSION

The key concept behind large-area single-crystal graphene growth is based on the idea that lateral growth of individual graphene nuclei may proceed unperturbed if neighboring nucleation sites are spaced widely apart. The kinetics of growing graphene under these conditions is subject to contradictory requirements, and it is not at all obvious how to create such growth conditions in terms of actual growth parameters.<sup>28,29</sup> Achieving extremely low nucleation density requires very low supersaturation of active carbon species, which is incompatible with generating the lateral growth rates necessary for rapid large-area growth. Currently there are no theoretical models, not even a conceptual picture, for performing graphene growth in this low nucleation regime.

The balance between nucleation and lateral growth is in general governed by the adsorption–desorption equilibrium of small hydrocarbon radical intermediate growth species C<sub>x</sub>H<sub>y</sub> ( $x \geq 1, y \geq 0$ ) that is controlled by the partial pressure (flow rate) of CH<sub>4</sub>.<sup>35–37</sup> The SEM images in Figure 1a illustrate the nucleation density and the graphene island size as a function of CH<sub>4</sub> flow rate for graphene grown in a standard CVD process on unoxidized Cu foils at 1040 °C and fixed growth time of 0.5 h. The nucleation density of CH<sub>4</sub> obtained from these images is plotted in Figure 1b as a function of flow rate. The simple exponential dependence in Figure 1b confirms that depletion of active nucleation sites follows first-order kinetics before coalescence occurs.<sup>31</sup> However, even in this regime the graphene island size exhibits a complex behavior as a function of the CH<sub>4</sub> flow rate, which is illustrated by the growth curve in Figure 1c. This curve describes the balance between the nucleation rate and the lateral graphene growth rate. The flow rate of 0.75 sccm of CH<sub>4</sub> is near the inflection point (arrow 1 in Figure 1c), above which the graphene island size decreases because it becomes dominated by the nucleation rate, which increases with the flow rate (compare panels for 0.75 and 1 sccm in Figure 1a). In this region full coverage is easily achieved, but the islands are small. The island size increases with decreasing CH<sub>4</sub> flow rate below 0.75 sccm and reaches a maximum (shown by the 0.5 sccm panel in Figure 1a) when an optimum balance is achieved between the nucleation and lateral growth rates (arrow 2). The largest islands grow in this region because both the nucleation rate and the lateral growth rate are moderate, allowing the islands to increase laterally until growth termination is reached. The very low CH<sub>4</sub> flow rates in the growth-limited

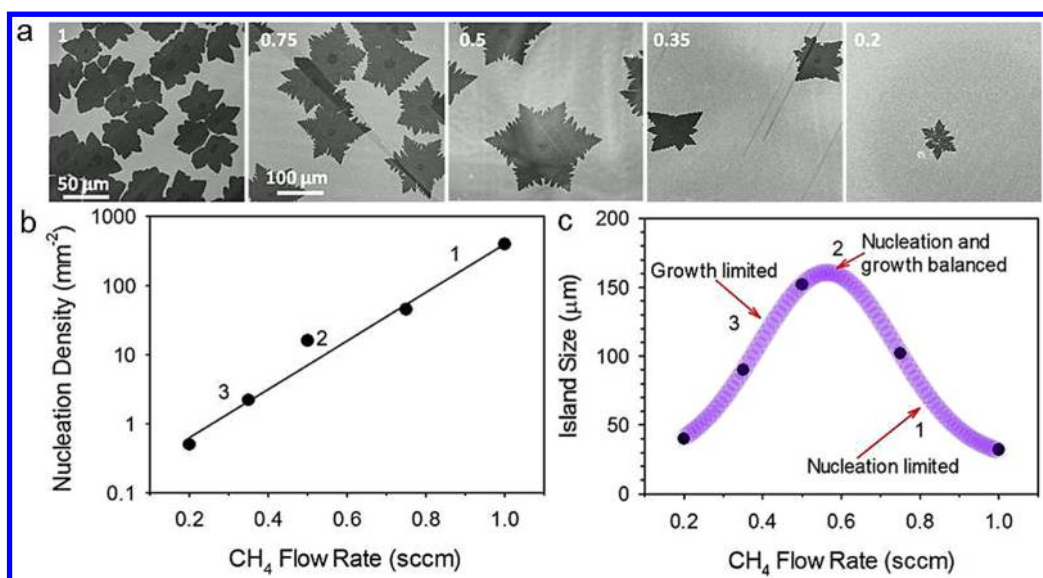


**Figure 1.** (a) SEM images of graphene grown under standard growth conditions and 0.5 h growth time. The numbers marking these images represent the flow rate of CH<sub>4</sub> in sccm. The 100 μm scale bar applies to the latter three images. (b) Nucleation density as a function of CH<sub>4</sub> flow rate. (c) Growth curve given by the graphene island size as a function of CH<sub>4</sub> flow rate, illustrating the three growth regimes described in the text.

regime below the maximum (arrow 3) of the curve produce a very low nucleation density. However, the onset of growth termination is also faster with decreasing CH<sub>4</sub> flow rates in this regime, precluding growth of large islands (compare panels for 0.35 and 0.2 sccm).

The growth curve in Figure 1c reveals that the window for optimal graphene growth is relatively narrow. This curve also shows that the graphene size cannot be increased indefinitely simply by reducing the CH<sub>4</sub> flow, because although nucleation can still occur, below some threshold value the always present parasitic processes take over, causing rapid growth termination. The mechanism of growth termination can include multiple processes, but the most likely are etching by hydrogen<sup>9,38</sup> and depletion of active graphene edge sites by reaction with background impurities in the growth environment, such as oxygen-containing species.<sup>29,30,39,40</sup> Although the diffusion and desorption rates both increase with temperature,<sup>41</sup> the typical growth temperatures in LPCVD graphene growth are already near the melting point of Cu, where the high evaporation rate of Cu produces undesirable transformations of the substrate itself<sup>42</sup> and the growth environment,<sup>41</sup> ruling out increasing the growth temperature as a viable option.

Although, the exact nature of the active nucleation sites is not known, it is understood that graphene preferentially nucleates at defects, impurities, kinks, scratches,<sup>41,43,44</sup> and step edges.<sup>45,46</sup> Controlling the concentration of these surface sites is typically the first step in reducing the graphene nucleation density. In agreement with published reports,<sup>41</sup> we show in Figure S9 that graphene nucleation on Cu foils occurs preferentially on or near rolling-induced features that may reach up to several micrometers in height.

The high-magnification SEM images in Figure S10 show close-ups of a few such graphene nucleation sites. The approach that has shown most promise for suppressing graphene nucleation is centered on reducing the surface roughness of the Cu foil by high-temperature annealing near or at the melting temperature of Cu.<sup>47–49</sup>

The two-step approach for reducing the nucleation site density used in this work starts with oxidation of the Cu foils. Standard 25 μm thick copper foils of 99.8% purity were solvent cleaned, loaded into an alumina boat in a quartz tube furnace, and oxidized in air for 15 min at temperatures ranging from 200 to 500 °C. A series of such oxidized foils prepared at different oxidation temperatures are shown in Figure S1. The optical images in Figure S2 illustrate a complex evolution of surface morphology by oxidation consisting of erosion and transformation of the rolling-induced texture of as-received foils and the appearance of a new microstructure, especially at 400 °C. The foils are designated by “f<sub>T</sub>” where f stands for foil and the subscript *T* represents the oxidation temperature. As-received unoxidized foils designated by RT, for room temperature, serve as control samples. The oxidized foils were reduced back to Cu by annealing at 1040 °C for up to 3 h in a H<sub>2</sub> atmosphere, maintained at 150 mTorr using a 10 sccm H<sub>2</sub> flow rate. X-ray diffraction (XRD) was used for characterizing the crystallographic orientation and the microstructure of the Cu foils as received, after oxidation, and after the hydrogen-annealing reduction step. The XRD data in Figure S4 show evolution of the grain orientation in the foils with temperature from a polycrystalline mixture of (100), (110), (111), and (311) grains found in as-received foils to dominantly (100) grains for foils oxidized above 400 °C. The Cu grains were up to a few millimeters

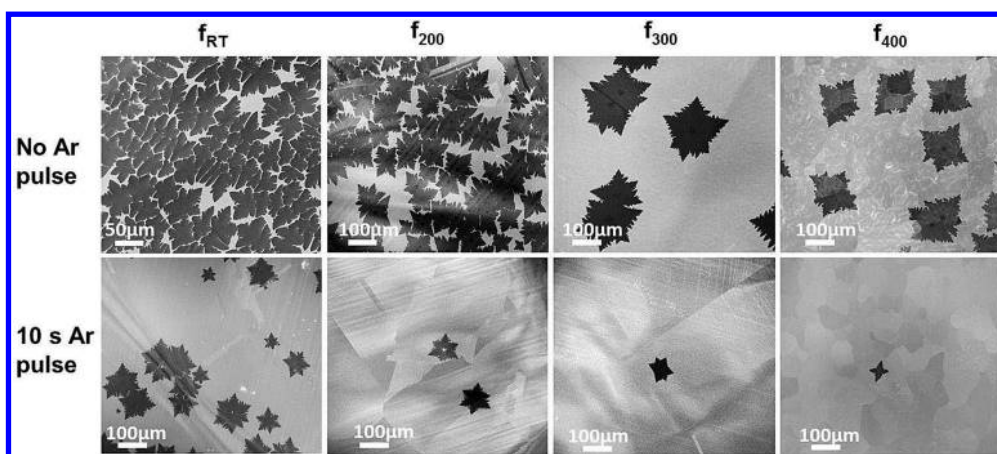


Figure 2. SEM images of Cu foils (denoted  $f_T$  where  $T$  is the oxidation temperature) after oxidation, hydrogen reduction at 1040 °C, and then graphene growth of 0.5 h at 1040 °C: (a–d) at 0.5 sccm  $\text{CH}_4$  without using an Ar pulse; (e–h) at 1.5 sccm  $\text{CH}_4$  with a 10 s duration Ar pulse applied at the onset of  $\text{CH}_4$  flow.

for  $f_{\text{RT}}$ ,  $f_{200}$ , and  $f_{300}$  foils. In contrast, in  $f_{400}$  and  $f_{500}$  foils smaller (50 to 300  $\mu\text{m}$ ) and more uniform (100) grains became dominant after the oxidation/reduction cycle.

Graphene CVD on these oxidized and reduced Cu foils was performed using the process described in a previous report<sup>4</sup> in continuation of the 3 h annealing/reducing treatment at 1040 °C. A set of samples selected to cover the entire range of oxidation temperatures was simultaneously exposed to a fixed flow rate of  $\text{CH}_4$  to rule out inadvertent variations in the growth conditions. Figure 2a–d show SEM images of graphene grown on Cu foils prepared at different temperatures by the oxidation/reduction cycle followed by 0.5 h growth at a 0.5 sccm  $\text{CH}_4$  flow rate. The sequence of SEM images shows a significant fall in the graphene nucleation density on the oxidized foils. A plot of the nucleation density as a function of the oxidation temperature is also shown in Figure 3. The images and the plot show that the nucleation density initially falls with increasing oxidation temperature. It reaches the lowest value at 300 °C, after which it develops a weak upward trend with increasing oxidation temperature. The nucleation density for the  $f_{300}$  foil is roughly 2 orders of magnitude lower than that for the  $f_{\text{RT}}$  foil. We find that the graphene nucleation density does not depend on the Cu grain orientation. This observation is in agreement with the report by Kim *et al.*,<sup>41</sup> and it is in contrast with the results reported by Wood *et al.*<sup>50</sup> The slightly higher nucleation density on  $f_{400}$  foils than that on  $f_{300}$  correlates with the increasing surface roughness starting above 300 °C as shown in Figure S3.

The overall mechanism of suppressing and deactivating the nucleation sites by oxidation has two main components: (1) the removal of surface impurities by oxidation and (2) the healing of mechanical defects by subsequent reduction, annealing, and regrowth of the oxidized foils. The temperature dependence of the nucleation density in Figure 3 suggests that the oxidation step and regrowth of the Cu layer during the subsequent

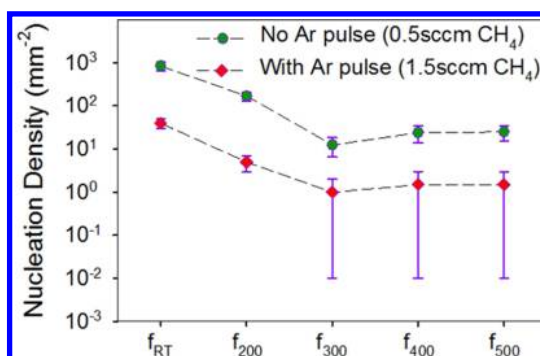


Figure 3. Graphene nucleation density on Cu foils oxidized at the indicated temperatures and reduced at 1040 °C in hydrogen, with and without application of a 10 s duration Ar pulse during introduction of  $\text{CH}_4$ . Graphene growth for 0.5 h at 1040 °C was performed at 0.5 sccm  $\text{CH}_4$  without the Ar pulse and at 1.5 sccm  $\text{CH}_4$  with the Ar pulse. The dashed lines are guides to the eye.

reduction step combine into a more effective method for reducing the nucleation density than  $\text{H}_2$  annealing alone described by the  $f_{\text{RT}}$  foils. The nucleation density also falls because oxidation removes exogenous carbon accumulated on the Cu foils during processing, which has been found to promote graphene nucleation and create multi-layer regions.<sup>41</sup> Although Figures 2 and 3 show that oxidation of the Cu foils before annealing in  $\text{H}_2$  is highly effective in reducing nucleation site density, this treatment alone is unable to completely suppress nucleation of graphene on Cu. The new method described in the second step is capable of fully suppressing graphene nucleation.

The second step for reducing the nucleation density is based on interacting directly with the growth process at the time of nucleation. This interaction is accomplished by using a brief Ar pulse at the onset of growth, referred to as transient reactant cooling. It is well established that most graphene nucleation occurs during the initial exposure of the Cu surface to  $\text{CH}_4$ .<sup>14,41</sup> The transient reactant cooling is performed by using a 10 s duration pulse of Ar that causes the pressure in the



CVD tube to rise to about 1 Torr. The Ar pulse is applied concurrently with the start of the CH<sub>4</sub> flow at the onset of growth. The most intriguing result of using the Ar pulse is that it can completely suppress nucleation of graphene. Under the conditions of 0.5 h growth at 0.5 sccm CH<sub>4</sub> flow used with the oxidized foils no nucleation is observed on any of the Cu foils. To recover nucleation on the Cu foils when applying the Ar pulse, we gradually increased the CH<sub>4</sub> flow and found that at roughly  $3 \times 0.5 = 1.5$  sccm CH<sub>4</sub> flow nucleation occurs again. Growth with the Ar pulse is illustrated by the SEM images in Figures 2e–h, showing graphene on Cu foils after 0.5 h of growth. The plot in Figure 3 shows that the application of the Ar pulse produces a roughly 1 order of magnitude decrease in the nucleation site density, in addition to the already 2 orders of magnitude decrease produced by the oxidation/reduction cycle. Note that the large error bars at low nucleation density are not an artifact, but a manifestation of the stochastic nature of the nucleation process.<sup>31</sup> The consequence of the inherent randomness is that it is not possible to limit growth reproducibly to only a single site by methods based on controlling nucleation to start the growth process.<sup>51</sup>

The transient reactant cooling step is different from all previously used approaches for suppressing nucleation because of its dynamic nature. The 1 order of magnitude decrease of the nucleation density in Figure 3 produced by the Ar pulse corresponds to an effective increase in the activation barrier of  $\Delta E_a = k_B T \ln(10) \approx 0.25$  eV, where  $k_B$  is the Boltzmann constant and  $T \approx 1300$  K the growth temperature. The use of transient cooling is based on the general principle that nucleation requires much higher supersaturation than growth.<sup>41</sup> The nucleation of graphene is particularly favorable for this approach because according to recent experimental and theoretical reports the critical nucleus—instead of two or three atoms that is typical for metals—includes six carbon clusters, the formation of which requires a correspondingly much higher supersaturation of reactive carbon species.<sup>52</sup> In addition, the growth of critical size clusters after their formation rapidly accelerates the depletion of reactive carbon species, producing a large drop in supersaturation. Unless this loss is compensated by deliberately increasing the concentration of reactive species, the critical supersaturation necessary for nucleation cannot be reached again. The purpose of using transient reactant cooling is to generate a temporary jump in the effective nucleation barrier to force the nucleation step to occur at much lower nucleation densities. The finite drop in the nucleation density shown by the plot in Figure 3 confirms that no new nucleation occurs after the temperature in the reactor is restored to its initial value prior to the Ar pulse.

We suggest that the main molecular mechanism behind transient reactant cooling is the deactivation of the hydrocarbon growth species by collisions with Ar

atoms in which a substantial amount of vibrational energy is transferred out of activated carbon species into translation of the Ar atoms.<sup>32</sup> The collisions with Ar atoms and the resulting deactivation can affect both the reactive species in the gas phase and those on the growing surface. Considering that graphene growth occurs by a surface-limited reaction, the rest of the discussion concerns only reactive intermediates forming on the growing surface. To estimate the effectiveness of CD on the critical cluster formation, we use the example of similar molecular structures for which CD studies have been performed.<sup>33,34</sup> For an order of magnitude type estimate of the efficiency of CD, it is sufficient to know the type of molecular structures, which determine the properties of the vibrational energy manifolds affected, without actually identifying the specific molecular species. The recent scanning tunneling microscopy (STM) imaging and spectroscopy (STS) measurements<sup>53,54</sup> and theoretical modeling<sup>55</sup> found the intermediates for the critical cluster formation of graphene to be aggregates of hexagonal and pentagonal ring structures that belong to the class of small aromatic hydrocarbons. These results reveal that the chemical pathways for the formation of the critical cluster share great similarity with the pathways for the formation of aromatic hydrocarbons that have been extensively studied in connection with combustion processes.<sup>56</sup> From the main intermediates in combustion processes we selected azulene<sup>33</sup>—a molecule that consists of a pentagonal and a hexagonal ring fused together—as the representative of the intermediate structures in the graphene critical cluster formation. Azulene has been extensively used as a model system for studying the mechanism and the efficiency of CD in highly vibrationally excited molecules.

The key reason why the Ar pulse is effective in reducing the nucleation density is related to a specific feature of the CD mechanism. Extensive experimental and theoretical studies of CD have shown that the average energy transferred ( $\Delta E$ ) per collision increases roughly linearly with the total vibrational energy of the molecule.<sup>33</sup> This means that collisions with inert gas atoms are most effective in reducing the reactivity near or at the reaction threshold. Using the experimental data for azulene CD,<sup>33</sup> and 2.6 eV as the value for the activation energy for the nucleation of graphene,<sup>41</sup> gives  $\Delta E = 0.12$  eV for the estimated energy transferred out of azulene after a single collision with Ar. This value can be used to estimate the effect of deactivating collisions on the nucleation of graphene using the Boltzmann factors for population probabilities as an approximation for the concentration of reactive species below and at the threshold. The ratio of the Boltzmann factors for an energy difference equal to  $\Delta E = 0.12$  eV at the activation energy barrier for nucleation gives  $P(E_a = 2.48)/P(E_a = 2.6) \propto \exp(-0.12/k_B T) = 0.33$  at a growth temperature of  $T \approx 1300$  K. This ratio is

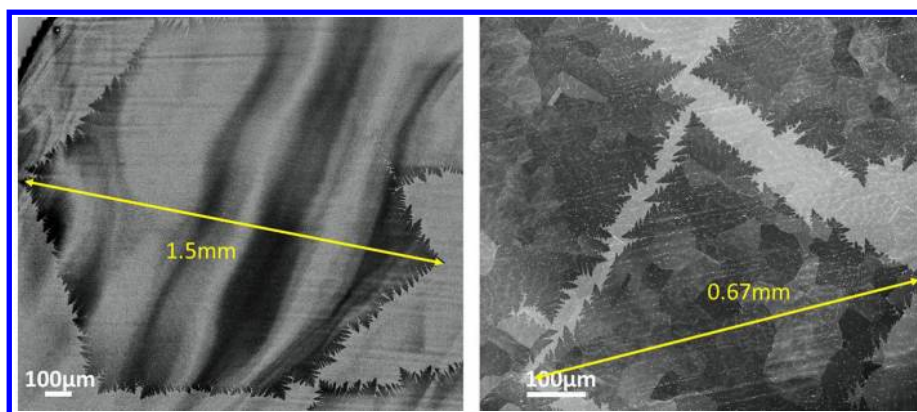


**Figure 4.** Millimeter-scale graphene grains grown in 2 h by the two-step nucleation density reduction approach on two Cu foils that were oxidized at (a) 300 °C and (b) 400 °C. Note that the graphene grains change shape from hexagonal on  $f_{300}$  to rectangular on  $f_{400}$ .

close to the factor of 3 by which the  $\text{CH}_4$  flow rate has to be increased in our experiments to recover nucleation after the application of the Ar pulse. An additional benefit of having to increase the  $\text{CH}_4$  flow rate by a factor of 3 is that the lateral growth rate in the postnucleation stage of the growth is boosted proportionally despite a drop in supersaturation that occurs because the reaction zone surrounding the growing grains is gradually depleted of active species.

If the growth time is extended to an hour after the Ar pulse, the control foil  $f_{\text{RT}}$  becomes uniformly covered because of the coalescence of graphene grains grown at high nucleation density. However, the additional 0.5 h of growth leaves the nucleation density on  $f_{300}$  and  $f_{400}$  foils unchanged. In addition, the factor of 3 increase in the  $\text{CH}_4$  flow causes a substantial increase in the lateral growth rate of the grains. The combination of low nucleation density and high lateral growth rate enables the growth of millimeter-size graphene grains on  $f_{300}$  prepared foils. The largest graphene grain of 1.5 mm grown under these conditions is shown in Figure 4, with additional SEM images of large grains provided in Figure S6. All the graphene grains are single layer except near the nucleation centers and around impurity particles, where double or multiple layers were observed occasionally, as shown in Figure S7. The additional contrast in the graphene grains on  $f_{400}$  in Figure 4b comes from the grain structure of the underlying Cu foil and not from the presence of multilayer flakes of graphene.<sup>24</sup> After 2 h of continuous growth at the same conditions these individual graphene domains coalesce together to form a uniform graphene layer on all the oxidized and reduced Cu foils, as shown in Figure S8.

Selected area electron diffraction (SAED) was used to confirm that the large graphene grains are single crystal.<sup>7,22,24,27,28</sup> Multiple SAED patterns were taken from different locations on suspended graphene films (both hexagonal and rectangular grains) transferred onto gold TEM grids. The position of a few SAED patterns taken from hexagonal graphene grains shown

in Figure 5 is identified by the color-coordinated dots and image frames in a clockwise direction.

The orientation of the SAED patterns in Figures 5c–e remains unchanged with distance, confirming the single crystal lattice structure. The largest linear dimension of this single-crystal grain obtained from the distance between the red and the purple dots is roughly 1 mm. In comparison, the SAED pattern from a neighboring graphene grain in Figure 5f is rotated roughly by 90°, revealing that it comes from a different domain.

Using standard procedures, a few of the graphene films were also transferred to Si substrates with a 300 nm thick  $\text{SiO}_2$  for characterization by Raman spectroscopy to assess further their quality, uniformity, and the number of layers.<sup>57</sup> The excitation wavelength was 633 nm, and Raman spectra were collected from different locations and over large areas in a mapping mode. Figure 6a and b show the Raman spectra taken from different locations from both hexagonal and rectangular graphene grains. Both types of grains show a low D peak intensity at  $1330\text{ cm}^{-1}$ , typical of high-quality graphene films. The edges shown by the red spectra in Figure 6a and b have a slightly higher D peak intensity because of reduced symmetry and a higher likelihood for defect formation at these locations.<sup>58</sup> The 2D peak is symmetric and has a narrow line width around  $30\text{ cm}^{-1}$ . The ratio of 2D to G peak intensity is 2 or more, confirming single-layer graphene.<sup>1,57</sup> Raman mapping performed on a  $35 \times 40\text{ }\mu\text{m}^2$  corner of a large graphene grain is shown in Figure 6c–e. Maps were extracted for D, G, and 2D peak intensities at 1330, 1585, and  $2650\text{ cm}^{-1}$ , respectively. Note that background subtraction was performed in all cases. Other than at the edges, the D peak has negligible intensity, although some of the defective regions in the form of holes and folds may have been created by the transfer process. Except for a transfer-induced hole, the 2D and G peak intensities are quite uniform over the entire mapped region, and their ratio is between 2 and 3, confirming the uniformity of the

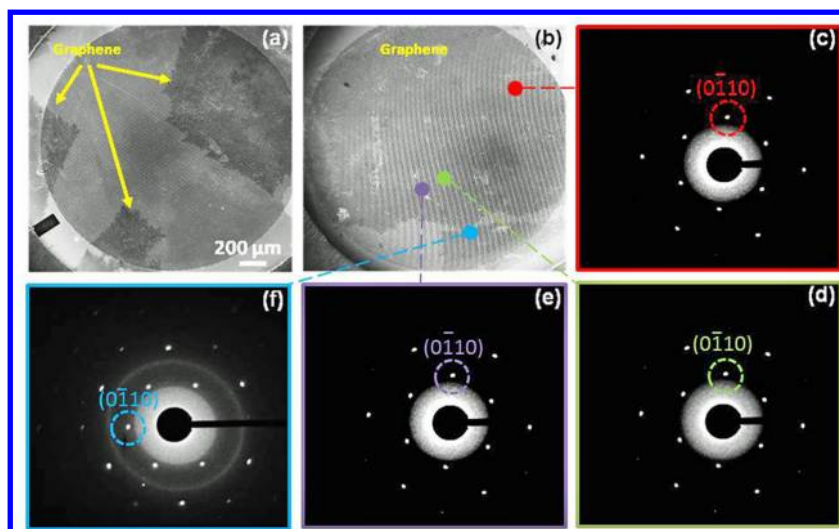


Figure 5. Selected area electron diffraction from suspended graphene films transferred onto a gold grid. (a and b) The darker regions in these SEM images represent the suspended graphene. (c–e) SAED patterns from a single graphene grain designated by colored dots showing the same orientation. (f) SAED pattern from neighboring grain showing significant rotation.

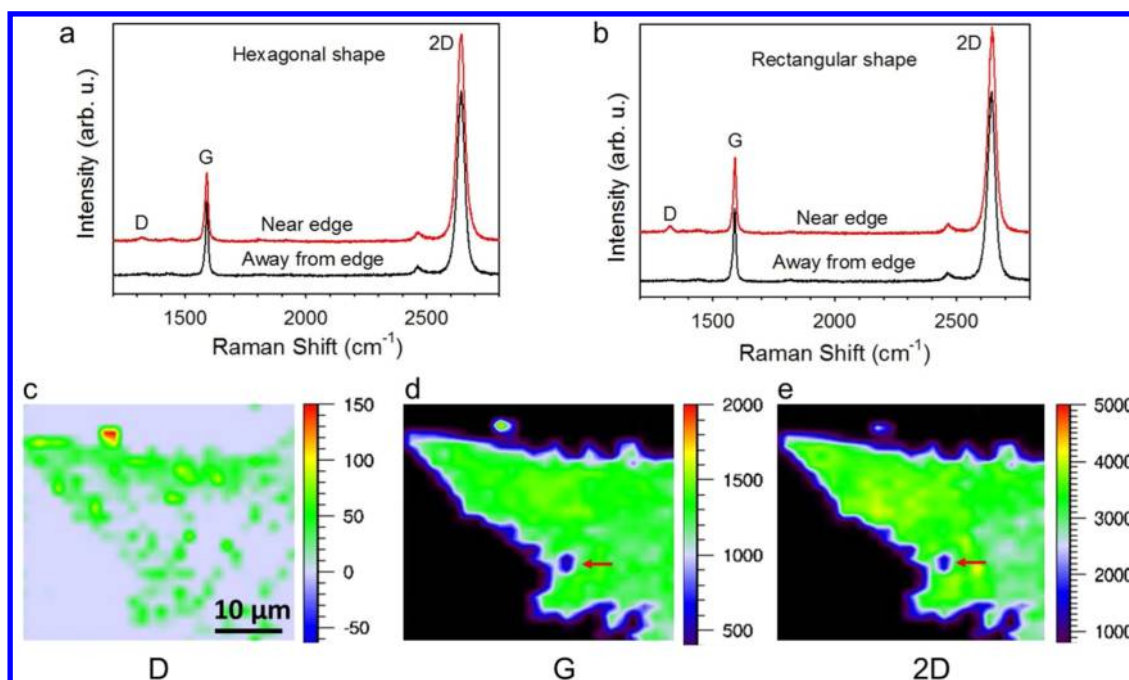
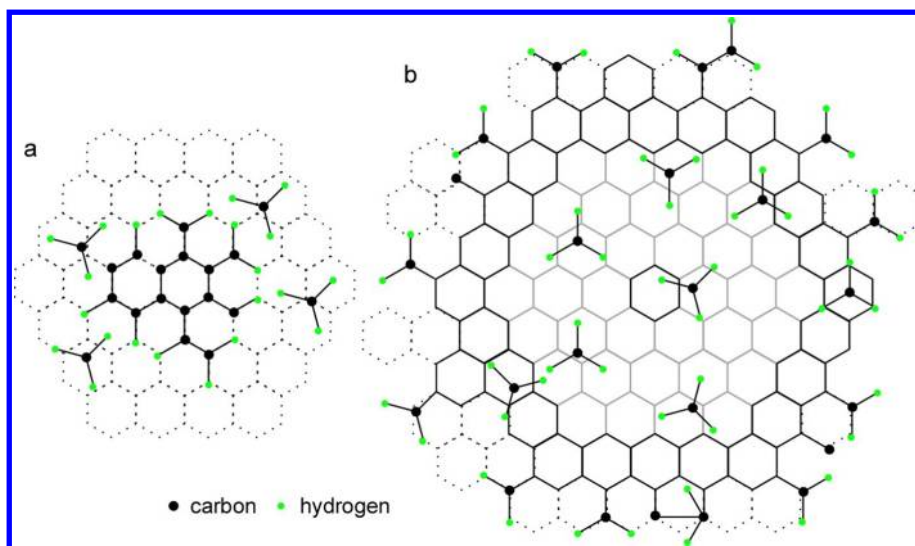


Figure 6. Raman spectra and Raman maps of graphene films transferred on 300 nm  $\text{SiO}_2/\text{Si}$  measured using 633 nm excitation. (a) Raman spectra from hexagonal graphene grains grown on  $f_{300}$  obtained at the edge and away from the edge. (b) Raman spectra from rectangular graphene grains grown on  $f_{400}$  obtained at the edge and away from the edge. On both graphene grains the edge is more defective. (c–e) Raman maps for D, G, and 2D peaks measured at a corner of a rectangular graphene grain. The red arrow shows a hole produced during transfer.

single-layer graphene. The small variations observed in the peak intensities, peak positions, and the line width are caused by local variations in unintentional doping by physisorbed species from atmospheric contaminants, substrate–graphene interactions, local strain, wrinkles, and local defects in the transferred graphene.<sup>4,59–61</sup>

The change of the shape of the graphene grains is a strong indication that the oxidation–reduction treatment alters key properties of the original Cu foil that

affect graphene growth. The graphene grains grown on  $f_{\text{RT}}$ ,  $f_{200}$ , and  $f_{300}$  treated foils have mostly hexagonal symmetry (six lobes), as shown in Figure 2a–c and e–g and Figure 4a. A small number of rectangular domains with four lobes were also observed on these foils. The  $f_{400}$  and  $f_{500}$  treated foils show exclusively rectangular symmetry with four lobes, as illustrated in Figures 2d,h and 4b.<sup>62,63</sup> In general, there are three factors that differentiate the Cu foils in graphene growth: (1) crystallographic orientation of the grains, (2) surface



**Figure 7.** (a) Illustration of the binding of reactive IPM carbon species at the dashed hexagonal grid junctions in graphene nucleation. (b) Growth of graphene according to the Eden cluster model showing in light gray a completed compact inner region surrounding a single nucleus illustrated by the dark hexagonal ring, and a still growing incomplete outer ring of the graphene island. The methyl radicals in the schematic illustrate a generic growth species. IPMs attach at the edge and a few EPs are shown randomly distributed on the top of the island.

microstructure, and (3) Cu grain size or density of grain boundaries.<sup>50,62–66</sup> On the basis of previously published work and our results here, we can rule out some of these factors.<sup>62</sup> Since graphene growth on all foils was carried out in a batch mode in a single experiment, the effects of inadvertent variation in the growth conditions,<sup>27</sup> such as etching by hydrogen,<sup>9,38</sup> can be ruled out. Previous reports have established that the interaction between the Cu surface and the graphene is relatively weak.<sup>48,67–73</sup> In agreement with these reports, we also find that the effect of the grain boundaries is negligible since graphene grains grow unperturbed across grain boundaries.<sup>7</sup> However, on the basis of Cu grains “visible” through the graphene layer in Figure 4b, definite alignment of the outer edges of the graphene patch and the Cu grain edges can be inferred. This conclusion is supported by the XRD data, which show that the smaller Cu grains on  $f_{400}$  foils have a predominantly (100) texture, suggesting that the crystallographic orientation of the Cu grains influences the shape of the graphene crystals. The important conclusion that can be drawn from these results is that the crystallographic orientation of the Cu grains is not a factor that dramatically changes the nucleation density up or down, but as revealed by Figure 4a and b, it can be a decisive factor for enabling graphene grains to grow faster and larger by promoting preferential nucleation of hexagonal-shape grains over rectangular grains.

We use a kinetic model to explore the possible mechanisms of graphene growth as a function of the nucleation density. In its simplest form graphene growth occurs on a hexagonal grid that represents the active sites for graphene formation on a flat surface. The binding of carbon atoms at the active sites shown in Figure 7a occurs from reactive carbon

intermediates  $C_xH_y$  ( $x \geq 1$ ,  $y \geq 0$ ) that are produced by the decomposition of  $CH_4$  molecules on the Cu surface.<sup>53–55</sup> The rate of chemisorption of reactive carbon species ( $dC/dt$ ) is proportional to the impingement rate  $J$  at a single site, the probability of binding at the grid sites  $s$ , and the concentration of free surface sites:

$$dC/dt = sJC(t)[C_0 - C(t)]/C_0 \quad (1)$$

After substituting  $\theta(t) = C(t)/C_0$  for the surface coverage an equation for the variation of the graphene coverage  $\theta$  is obtained where  $s$  now corresponds to the sticking coefficient of reactive carbon species:

$$d\theta/dt = sJ\theta(t)[1 - \theta(t)] \quad (2)$$

The variation in the graphene growth rate observed in experimental measurements indicates that the overall sticking coefficient  $s$  is not constant.<sup>14</sup> The overall sticking coefficient must account for both chemisorption of carbon species that occurs at vacant substrate sites and chemisorption of carbon species that occurs above already existing islands. The presence of two types of precursor species was first discussed by Kisliuk in connection with molecular chemisorption processes.<sup>74–76</sup> But, in a recent report it was shown that such precursor species can have a more general significance extending to the epitaxial growth of thin films.<sup>77</sup> The sticking coefficient designated by  $s_0$  describes the mechanism for capturing the active species at random vacant sites; these species are referred to as intrinsic precursor molecules (IPMs). The IPM component is described by a Langmuir form with the sticking coefficient proportional to the fraction of empty sites given by  $s_0(1 - \theta(t))$ . The second sticking coefficient designated by  $s_1$  describes the physisorption of active



species on top of already formed graphene islands. These species are referred to as extrinsic precursor molecules (EPMs). The EPMs provide direct contribution to island growth by random jumps until a vacant chemisorption site is found. Since the attractive adsorbate–adsorbate interactions are strongest near island edges, the incorporation of EPMs is most likely to occur at already existing islands. The EPM component of chemisorption is described by a coverage-dependent sticking coefficient that is proportional to both the concentration of reactive species and the free surface area available for adsorption given by  $s_1\theta(t)[1 - \theta(t)]$ . After addition of the random nucleation component  $s_0(1 - \theta(t))$  to eq 2 it becomes

$$d\theta/dt = J\{s_0[1 - \theta(t)] + s_1\theta(t)[1 - \theta(t)]\} \quad (3)$$

where the coverage-dependent sticking coefficient  $s(\theta) = s_0[1 - \theta(t)] + s_1\theta(t)[1 - \theta(t)]$  describes the overall contribution by both precursor types. The solution to this differential equation is obtained after rearranging eq 3 to

$$d\theta/dt = [1 - \theta(t)][\theta_0 + \theta(t)]/[\tau(1 + \theta_0)] \quad (4)$$

where  $\theta_0 = s_0/s_1$  describes the ratio of the sticking coefficients, and  $\tau = 1/J(s_0 + s_1)$  describes the scaled binding time at a single adsorption site that depends on both sticking coefficients and the impingement rate that is proportional to the concentration of active carbon species determined by the  $\text{CH}_4$  flow rate. The solution of this differential equation is given by

$$\theta(t) = 1 - (1 + \theta_0)/(1 + \exp[(t - t_0)/\tau]) \quad (5)$$

where  $t_0$  is an integration constant given by  $\theta(0) = 0$ . The solution corresponds to a family of sigmoidal S-shaped growth curves that describe the different growth regimes as a function of the flux of growth species given by  $\tau$  and the ratio of sticking coefficients  $\theta_0$ . The illustration of the solutions in Figure 8 reveals that the dominant growth mechanism can be deduced from the shape of growth curves that is determined by the ratio of the sticking coefficients  $s_0/s_1$ . The two important limiting cases of the solution occur for  $\theta_0 \gg 1 \Rightarrow s_0 \gg s_1$ , corresponding to nucleation-dominated growth, and for  $\theta_0 \ll 1 \Rightarrow s_1 \gg s_0$ , corresponding to the island growth-dominated regime. The solution for  $\theta_0 \gg 1$  has a simplified form,  $\theta(t) = 1 - \exp(-t/\tau)$ , resulting in the red growth curve recognizable by its highly asymmetric shape. As the magnitudes of the two sticking coefficients approach each other, the growth curve becomes more symmetric, first going through an inflection point for  $\theta_0 = 1 \Rightarrow s_1 = s_0$ , and finally acquiring the fully symmetric sigmoidal profile given by the black line and the simplified equation  $\theta(t) = 1/[1 + \exp(-t/\tau)]$  for  $\theta_0 \ll 1$ .

The plot in Figure 8 also compares experimental data corresponding to the island growth-dominated regime from this work shown by the black solid dots

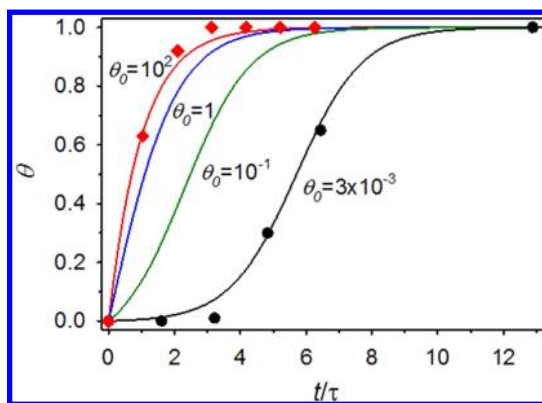


**Figure 8.** Variation of the shape of the growth curves given by eq 5 with the ratio of sticking coefficients  $\theta_0$  covering a range from  $10^2$  to  $3 \times 10^{-3}$ . The nucleation-dominated regime is described by  $\theta_0 \gg 1$ , and the island growth regime by  $\theta_0 \ll 1$ . Red diamonds represent data from ref 14, and black solid dots are experimental data from this work.

with experimental data for the nucleation-dominated regime obtained from the literature given by the red diamonds.<sup>14</sup> Additional data in this reference show that, as our model predicts, the growth curves become steeper with increasing  $\text{CH}_4$  concentration ( $\theta_0 \gg 1$ ). The experimental data are used to extract the sticking coefficients in the growth experiments and compare them with those obtained from independent surface science measurements. By fitting a sigmoidal function to the raw experimental data shown in Figure S12 a value of 560 s is obtained for  $\tau$ . Using the solution given by eq 5 to fit the data plotted in Figure 8 as a function of the dimensionless parameter  $t/\tau$  gives  $\theta_0 = 3 \times 10^{-3}$ , a value in line with precursor-mediated adsorption mechanisms. From the partial pressure of 20 mTorr of  $\text{CH}_4$  used in the growth experiments and the simplified equation of  $\tau = 1/Js_1$  a value of  $s_1 = 0.03$  is obtained. Finally, using  $\theta_0 = 3 \times 10^{-3}$  gives  $9 \times 10^{-5}$  for the value of  $s_0$ . These values indicate that the change in the methane chemisorption mechanism from an IPM to an EPM is accompanied by a roughly 3 orders of magnitude increase in the sticking coefficient. The very low  $\text{CH}_4$  sticking coefficient  $s_0$  is in good agreement with values reported in the literature for independent surface science measurements indicative of the low reactivity of  $\text{CH}_4$  on Cu and metal surfaces in general.<sup>39,78</sup> The theoretical explanation of the low sticking coefficients is that the catalytic dissociation of the C–H bond in  $\text{CH}_4$  is dominated by tunneling from a molecular precursor in thermal equilibrium with the surface.<sup>78</sup>

However, the most remarkable implication of the graphene growth kinetic model corresponds to the special case for  $s_0 = 0$  for which the solution of the differential equation is identically zero,  $\theta(0) = 0$ , meaning that for growth to occur, nucleation must always exist. This solution implies that a special two-dimensional island growth mechanism must exist from the onset since the only active sites available for carbon incorporation are those at the edge of a very

few nuclei. Initially, this cooperative process is less efficient than random nucleation, as the slowly rising part of the S-shaped growth curve at very low coverages shows in Figure 8. We propose to use the Eden cluster model as a framework for illustrating how carbon incorporation by this cooperative growth mode occurs. The Eden model provides a general picture for the formation of a compact two-dimensional structure (2D) that starts growing from a single nucleation site by random addition of growth species at its perimeter.<sup>79</sup> The spontaneous growth at the island boundary leads to formation of compact aggregates with  $L \approx A^{1/2} \approx K^{1/2}$  describing the relationship between the perimeter length ( $L$ ), the area ( $A$ ), and the number of particles ( $K$ ) in the Eden cluster.<sup>80</sup> In contrast to random aggregation, the Eden cluster formation has a built-in mechanism for taking into consideration lateral positional correlation between the carbon growth species and the growing graphene. This correlation originates from the conversion of the EPM to IPM when it is adsorbed at a vacant site near the edge of the island.

The Eden cluster model is ideally suited for treating two-dimensional crystallization such as in graphene because it naturally localizes growth to the outer edges of the island, where carbon incorporation chemistry is known to occur.<sup>41,81</sup> Figure 7b illustrates a simple example of a graphene Eden cluster that isotropically expands its diameter by random addition of carbon at the perimeter. A fully quantitative model that is currently under development includes the interaction with the grid dictated by the crystallographic properties of the substrate as the driving force for treating anisotropic growth that leads to the variety of shapes observed experimentally.<sup>64,65</sup> Finally, the edge of a growing cluster contains a large number of dangling bonds that are active sites for incorporation of carbon. Such active sites propagate the growth by dehydrogenation and ring closure reactions that occur by incorporation of a wide range of hydrocarbon species that can contain one to a few carbon atoms.<sup>56,82,83</sup> A chemically more refined version of the model can also be developed to explore the effects of carbon incorporation in a zigzag or armchair configuration on the shape of the islands.<sup>58,81</sup> The quantitative model is designed to address defect formation as a result of imperfect ordering during growth that can lead to grain boundary formation even in growth that starts from a single nucleation site that excludes coalescence-induced grain boundaries.<sup>84</sup>

## CONCLUSION

In summary, we explore the role that the nucleation density plays in determining the mechanism of

single-crystal graphene growth. To suppress the nucleation of graphene, we supplement the already established methods of pretreatment of the Cu foils using oxidation and reduction by H<sub>2</sub> annealing with a new method for reducing nucleation density that interacts directly with the growth process called transient reactant cooling. Transient reactant cooling is performed by an Ar pulse to produce collisional deactivation of the active carbon growth species at the remaining nucleation sites. An important feature of transient reactant cooling is that in contrast to the Cu foil pretreatment methods it is capable of completely suppressing nucleation of graphene. It is shown that to recover nucleation when the Ar pulse is used, the CH<sub>4</sub> flow rate has to be increased by a factor of 3 while keeping all other parameters unchanged. This two-step approach was used to obtain 3 orders of magnitude overall reduction in the nucleation density. We use a kinetic model to show that the extremes of the nucleation density range are associated with distinctly different graphene growth mechanisms. These extremes are clearly distinguishable by the different shapes of the growth curves that describe the coverage dependence in graphene growth. In the high nucleation density regime graphene growth occurs by coalescence of a large number of small islands. This growth regime is clearly undesirable because of the formation of a large number of grain boundaries. At vanishingly low nucleation density the growth mode changes to a cooperative island growth mechanism for carbon incorporation that occurs at the edges of existing islands. This is the mechanism where the boost in the CH<sub>4</sub> flow rate becomes particularly beneficial for increasing the lateral growth rate of graphene. The cooperative island growth mechanism intrinsically produces large-area single-crystal graphene. The kinetic model shows that the change in the growth mechanism occurs by a roughly 3 orders of magnitude increase in the reactive sticking probability of methane from  $5 \times 10^{-9}$  for random nucleation to 0.03 for cooperative island growth of graphene. The concepts developed in this work generalized by the kinetic model serve as a framework for optimization of the graphene CVD growth process for large-area single-crystal growth. The model also reveals that the upper limit to the size of graphene is ultimately imposed by the stochastic nature of the nucleation process. The kinetic model is not material specific. It is applicable to two-dimensional crystallization of any material system subject to strongly attractive adsorbate–adsorbate interactions.

## METHODS

As-received foils from Alfa Aesar, 99.8% Cu 25  $\mu$ m thick, were first oxidized in open air using a quartz tube furnace. The

experiments were performed in a 36 in. long quartz tube of 1 1/2 in. diameter with a 12 in. long heated region. The degree of oxidation was determined from XRD data. An oxidation time of

15 min was set to ensure that the foils are not oxidized through, preserving some of the original grains in the foils that serve as seeds in preferential regrowth of Cu during the H<sub>2</sub> annealing/reduction step. The oxidized Cu foils were placed in a Cu-coated alumina boat and batch annealed at 1040 °C in a quartz tube furnace for 3 h in a 10 sccm H<sub>2</sub> flow at 150 mTorr. Graphene growth was carried out by starting the CH<sub>4</sub> flow at either 0.5 or 1.5 sccm in the same tube furnace following completion of the annealing/reduction step of the Cu foils. Transient reactant cooling was performed by using a brief Ar pulse concurrently with starting the CH<sub>4</sub> flow that raises the total pressure to 1 Torr. The pressure after 10 s settles back to a slightly higher growth pressure of 165 mTorr from the addition of CH<sub>4</sub>. We confirmed that the position of the Cu foil has no effect on the outcome of the transient reactant cooling step by performing tens of runs with the sample placed within 3 in. from the center of the hot zone. Following a preset growth time the furnace was rapidly cooled below 100 °C and the tube was vented with Ar.<sup>4</sup> The graphene islands grown on Cu foils were imaged by SEM. A few graphene films were suspended on gold grids using published methods<sup>13</sup> to perform SAED to confirm the single-crystal nature of the grains. Raman spectroscopy and mapping was performed on graphene films transferred<sup>2</sup> on Si wafers with a 300 nm thick SiO<sub>2</sub> layer. The Raman spectra were collected using a laser excitation wavelength of 633 nm. The Renishaw WIRE 3.4 software was used to extract the Raman maps, and ImageJ from NIH was used for image analysis and for determining the nucleation density and the average island size.

**Conflict of Interest:** The authors declare no competing financial interest.

**Acknowledgment.** The synthesis science is sponsored by the Materials Sciences and Engineering Division, Office of Basic Energy Sciences, U.S. Department of Energy. Characterization science including Raman spectroscopy and the SEM part of this research was performed at the Center for Nanophase Materials Sciences user facility, which is sponsored at Oak Ridge National Laboratory by the Scientific User Facilities (SUF) Division, U.S. Department of Energy.

**Supporting Information Available:** This material is available free of charge via the Internet at <http://pubs.acs.org>.

## REFERENCES AND NOTES

- Li, X. S.; Cai, W. W.; An, J. H.; Kim, S.; Nah, J.; Yang, D. X.; Piner, R.; Velamakanni, A.; Jung, I.; Tutuc, E.; *et al.* Large-Area Synthesis of High-Quality and Uniform Graphene Films on Copper Foils. *Science* **2009**, *324*, 1312–1314.
- Li, X. S.; Zhu, Y. W.; Cai, W. W.; Borysiak, M.; Han, B. Y.; Chen, D.; Piner, R. D.; Colombo, L.; Ruoff, R. S. Transfer of Large-Area Graphene Films for High-Performance Transparent Conductive Electrodes. *Nano Lett.* **2009**, *9*, 4359–4363.
- Sun, Z. Z.; Yan, Z.; Yao, J.; Beitler, E.; Zhu, Y.; Tour, J. M. Growth of Graphene from Solid Carbon Sources. *Nature* **2010**, *468*, 549–552.
- Regmi, M.; Chisholm, M. F.; Eres, G. The Effect of Growth Parameters on the Intrinsic Properties of Large-Area Single Layer Graphene Grown by Chemical Vapor Deposition on Cu. *Carbon* **2012**, *50*, 134–141.
- Bhavioripudi, S.; Jia, X. T.; Dresselhaus, M. S.; Kong, J. Role of Kinetic Factors in Chemical Vapor Deposition Synthesis of Uniform Large Area Graphene Using Copper Catalyst. *Nano Lett.* **2010**, *10*, 4128–4133.
- Lee, Y.; Bae, S.; Jang, H.; Jang, S.; Zhu, S. E.; Sim, S. H.; Song, Y. I.; Hong, B. H.; Ahn, J. H. Wafer-Scale Synthesis and Transfer of Graphene Films. *Nano Lett.* **2010**, *10*, 490–493.
- Yu, Q. K.; Jauregui, L. A.; Wu, W.; Colby, R.; Tian, J. F.; Su, Z. H.; Cao, H. L.; Liu, Z. H.; Pandey, D.; Wei, D. G.; *et al.* Control and Characterization of Individual Grains and Grain Boundaries in Graphene Grown by Chemical Vapor Deposition. *Nat. Mater.* **2011**, *10*, 443–449.
- Robertson, A. W.; Warner, J. H. Hexagonal Single Crystal Domains of Few-Layer Graphene on Copper Foils. *Nano Lett.* **2011**, *11*, 1182–1189.
- Vlassioug, I.; Regmi, M.; Fulvio, P.; Dai, S.; Datskos, P.; Eres, G.; Smirnov, S. Role of Hydrogen in Chemical Vapor Deposition Growth of Large Single-Crystal Graphene. *ACS Nano* **2011**, 6069–6076.
- Vlassioug, I.; Smirnov, S.; Regmi, M.; Surwade, S. P.; Srivastava, N.; Feenstra, R.; Eres, G.; Parish, C.; Lavrik, N.; Datskos, P.; *et al.* Graphene Nucleation Density on Copper: Fundamental Role of Background Pressure. *J. Phys. Chem. C* **2013**, *117*, 18919–18926.
- Bae, S.; Kim, H.; Lee, Y.; Xu, X. F.; Park, J. S.; Zheng, Y.; Balakrishnan, J.; Lei, T.; Kim, H. R.; Song, Y. I.; *et al.* Roll-to-Roll Production of 30-Inch Graphene Films for Transparent Electrodes. *Nat. Nanotechnol.* **2010**, *5*, 574–578.
- Li, X. S.; Cai, W. W.; Colombo, L.; Ruoff, R. S. Evolution of Graphene Growth on Ni and Cu by Carbon Isotope Labeling. *Nano Lett.* **2009**, *9*, 4268–4272.
- Huang, P. Y.; Ruiz-Vargas, C. S.; van der Zande, A. M.; Whitney, W. S.; Levendorf, M. P.; Kevek, J. W.; Garg, S.; Alden, J. S.; Hustedt, C. J.; Zhu, Y.; *et al.* Grains and Grain Boundaries in Single-Layer Graphene Atomic Patchwork Quilts. *Nature* **2011**, *469*, 389.
- Li, X. S.; Magnuson, C. W.; Venugopal, A.; An, J. H.; Suk, J. W.; Han, B. Y.; Borysiak, M.; Cai, W. W.; Velamakanni, A.; Zhu, Y. W.; *et al.* Graphene Films with Large Domain Size by a Two-Step Chemical Vapor Deposition Process. *Nano Lett.* **2010**, *10*, 4328–4334.
- An, J. H.; Voelkl, E.; Suk, J. W.; Li, X. S.; Magnuson, C. W.; Fu, L. F.; Tiemeijer, P.; Bischoff, M.; Freitag, B.; Popova, E.; *et al.* Domain (Grain) Boundaries and Evidence of “Twinlike” Structures in Chemically Vapor Deposited Grown Graphene. *ACS Nano* **2011**, *5*, 2433–2439.
- Hashimoto, A.; Suenaga, K.; Gloter, A.; Urita, K.; Iijima, S. Direct Evidence for Atomic Defects in Graphene Layers. *Nature* **2004**, *430*, 870–873.
- Kim, K.; Lee, Z.; Regan, W.; Kisielowski, C.; Crommie, M. F.; Zettl, A. Grain Boundary Mapping in Polycrystalline Graphene. *ACS Nano* **2011**, *5*, 2142–2146.
- Rutter, G. M.; Crain, J. N.; Guisinger, N. P.; Li, T.; First, P. N.; Stroscio, J. A. Scattering and Interference in Epitaxial Graphene. *Science* **2007**, *317*, 219–222.
- Yazyev, O. V.; Louie, S. G. Electronic Transport in Polycrystalline Graphene. *Nat. Mater.* **2010**, *9*, 806–809.
- Jauregui, L. A.; Cao, H. L.; Wu, W.; Yu, Q. K.; Chen, Y. P. Electronic Properties of Grains and Grain Boundaries in Graphene Grown by Chemical Vapor Deposition. *Solid State Commun.* **2011**, *151*, 1100–1104.
- Grantab, R.; Shenoy, V. B.; Ruoff, R. S. Anomalous Strength Characteristics of Tilt Grain Boundaries in Graphene. *Science* **2010**, *330*, 946–948.
- Li, X.; Magnuson, C. W.; Venugopal, A.; Tromp, R. M.; Hannon, J. B.; Vogel, E. M.; Colombo, L.; Ruoff, R. S. Large-Area Graphene Single Crystals Grown by Low-Pressure Chemical Vapor Deposition of Methane on Copper. *J. Am. Chem. Soc.* **2011**, *133*, 2816–2819.
- Petrone, N.; Dean, C. R.; Meric, I.; van der Zande, A. M.; Huang, P. Y.; Wang, L.; Muller, D.; Shepard, K. L.; Hone, J. Chemical Vapor Deposition-Derived Graphene with Electrical Performance of Exfoliated Graphene. *Nano Lett.* **2012**, *12*, 2751–2756.
- Wang, H.; Wang, G.; Bao, P.; Yang, S.; Zhu, W.; Xie, X.; Zhang, W.-J. Controllable Synthesis of Submillimeter Single-Crystal Monolayer Graphene Domains on Copper Foils by Suppressing Nucleation. *J. Am. Chem. Soc.* **2012**, *134*, 3627–3630.
- Geng, D. C.; Wu, B.; Guo, Y. L.; Huang, L. P.; Xue, Y. Z.; Chen, J. Y.; Yu, G.; Jiang, L.; Hu, W. P.; Liu, Y. Q. Uniform Hexagonal Graphene Flakes and Films Grown on Liquid Copper Surface. *Proc. Natl. Acad. Sci. U.S.A.* **2012**, *109*, 7992–7996.
- Wu, Y. M. A.; Fan, Y.; Speller, S.; Creeth, G. L.; Sadowski, J. T.; He, K.; Robertson, A. W.; Allen, C. S.; Warner, J. H. Large Single Crystals of Graphene on Melted Copper Using Chemical Vapor Deposition. *ACS Nano* **2012**, *6*, 5010–5017.
- Zhang, Y.; Zhang, L. Y.; Kim, P.; Ge, M. Y.; Li, Z.; Zhou, C. W. Vapor Trapping Growth of Single-Crystalline Graphene

- Flowers: Synthesis, Morphology, and Electronic Properties. *Nano Lett.* **2012**, *12*, 2810–2816.
28. Yan, Z.; Lin, J.; Peng, Z.; Sun, Z.; Zhu, Y.; Li, L.; Xiang, C.; Samuel, E. L.; Kittrell, C.; Tour, J. M. Toward the Synthesis of Wafer-Scale Single-Crystal Graphene on Copper Foils. *ACS Nano* **2012**, *6*, 9110–9117.
  29. Zhou, H. L.; Yu, W. J.; Liu, L. X.; Cheng, R.; Chen, Y.; Huang, X. Q.; Liu, Y.; Wang, Y.; Huang, Y.; Duan, X. F. Chemical Vapor Deposition Growth of Large Single Crystals of Monolayer and Bilayer Graphene. *Nat. Commun.* **2013**, *4*, 2096.
  30. Hao, Y. F.; Bharathi, M. S.; Wang, L.; Liu, Y. Y.; Chen, H.; Nie, S.; Wang, X. H.; Chou, H.; Tan, C.; Fallahazad, B.; et al. The Role of Surface Oxygen in the Growth of Large Single-Crystal Graphene on Copper. *Science* **2013**, *342*, 720–723.
  31. Ratsch, C.; Venables, J. A. Nucleation Theory and the Early Stages of Thin Film Growth. *J. Vac. Sci. Technol., A* **2003**, *21*, S96–S109.
  32. Levine, R.; Bernstein, R. *Molecular Reaction Dynamics and Chemical Reactivity*; Oxford University Press: USA, 1987; p 552.
  33. Shi, J.; Barker, J. R. Energy-Dependent Collisional Deactivation of Vibrationally Excited Azulene. *J. Chem. Phys.* **1988**, *88*, 6219–6227.
  34. Bernshtein, V.; Oref, I. Energy Transfer between Polyatomic Molecules II: Energy Transfer Quantities and Probability Density Functions in Benzene, Toluene, P-Xylene, and Azulene Collisions. *J. Phys. Chem. A* **2006**, *110*, 1541–1551.
  35. Zhang, W. H.; Wu, P.; Li, Z. Y.; Yang, J. L. First-Principles Thermodynamics of Graphene Growth on Cu Surfaces. *J. Phys. Chem. C* **2011**, *115*, 17782–17787.
  36. Kim, H.; Saiz, E.; Chhowalla, M.; Mattevi, C. Modeling of the Self-Limited Growth in Catalytic Chemical Vapor Deposition of Graphene. *New J. Phys.* **2013**, *15*, 053012.
  37. Gajewski, G.; Pao, C. W. Ab Initio Calculations of the Reaction Pathways for Methane Decomposition over the Cu (111) Surface. *J. Chem. Phys.* **2011**, *135*, 064707.
  38. Zhang, Y.; Li, Z.; Kim, P.; Zhang, L.; Zhou, C. Anisotropic Hydrogen Etching of Chemical Vapor Deposited Graphene. *ACS Nano* **2011**, *6*, 126–132.
  39. Alstrup, I.; Chorkendorff, I.; Ullmann, S. The Interaction of CH<sub>4</sub> at High-Temperatures with Clean and Oxygen Pre-covered Cu(100). *Surf. Sci.* **1992**, *264*, 95–102.
  40. Robinson, Z. R.; Ong, E. W.; Mowll, T. R.; Tyagi, P.; Gaskill, D. K.; Geisler, H.; Ventrice, C. A. Influence of Chemisorbed Oxygen on the Growth of Graphene on Cu(100) by Chemical Vapor Deposition. *J. Phys. Chem. C* **2013**, *117*, 23919–23927.
  41. Kim, H.; Mattevi, C.; Calvo, M. R.; Oberg, J. C.; Artiglia, L.; Agnoli, S.; Hirjibehedin, C. F.; Chhowalla, M.; Saiz, E. Activation Energy Paths for Graphene Nucleation and Growth on Cu. *ACS Nano* **2012**, *6*, 3614–3623.
  42. Paronyan, T. M.; Pigos, E. M.; Chen, G.; Harutyunyan, A. R. Formation of Ripples in Graphene as a Result of Interfacial Instabilities. *ACS Nano* **2011**, *5*, 9619–9627.
  43. Luo, Z. T.; Lu, Y.; Singer, D. W.; Berck, M. E.; Somers, L. A.; Goldsmith, B. R.; Johnson, A. T. C. Effect of Substrate Roughness and Feedstock Concentration on Growth of Wafer-Scale Graphene at Atmospheric Pressure. *Chem. Mater.* **2011**, *23*, 1441–1447.
  44. Han, G. H.; Gunes, F.; Bae, J. J.; Kim, E. S.; Chae, S. J.; Shin, H. J.; Choi, J. Y.; Pribat, D.; Lee, Y. H. Influence of Copper Morphology in Forming Nucleation Seeds for Graphene Growth. *Nano Lett.* **2011**, *11*, 4144–4148.
  45. Saadi, S.; Abild-Pedersen, F.; Helveg, S.; Sehested, J.; Hinnemann, B.; Appel, C. C.; Nørskov, J. K. On the Role of Metal Step-Edges in Graphene Growth. *J. Phys. Chem. C* **2010**, *114*, 11221–11227.
  46. Gao, J. F.; Yip, J.; Zhao, J. J.; Yakobson, B. I.; Ding, F. Graphene Nucleation on Transition Metal Surface: Structure Transformation and Role of the Metal Step Edge. *J. Am. Chem. Soc.* **2011**, *133*, 5009–5015.
  47. Kojima, R.; Susa, M. Surface Melting of Copper with (100), (110), and (111) Orientations in Terms of Molecular Dynamics Simulation. *High Temp. - High Pressures* **2002**, *34*, 639–648.
  48. Rasool, H. I.; Song, E. B.; Mecklenburg, M.; Regan, B. C.; Wang, K. L.; Weiller, B. H.; Gimzewski, J. K. Atomic-Scale Characterization of Graphene Grown on Copper (100) Single Crystals. *J. Am. Chem. Soc.* **2011**, *133*, 12536–12543.
  49. Hoehne, K.; Sizmann, R. Volume and Surface Self-Diffusion Measurements on Copper by Thermal Surface Smoothing. *Phys. Status Solidi A* **1971**, *5*, 577–589.
  50. Wood, J. D.; Schmucker, S. W.; Lyons, A. S.; Pop, E.; Lyding, J. W. Effects of Polycrystalline Cu Substrate on Graphene Growth by Chemical Vapor Deposition. *Nano Lett.* **2011**, *11*, 4547–4554.
  51. Goh, L.; Chen, K. J.; Bhamidi, V.; He, G. W.; Kee, N. C. S.; Kenis, P. J. A.; Zukoski, C. F.; Braatz, R. D. A Stochastic Model for Nucleation Kinetics Determination in Droplet-Based Microfluidic Systems. *Cryst. Growth Des.* **2010**, *10*, 2515–2521.
  52. Zangwill, A.; Vvedensky, D. D. Novel Growth Mechanism of Epitaxial Graphene on Metals. *Nano Lett.* **2011**, *11*, 2092–2095.
  53. Niu, T. C.; Zhou, M.; Zhang, J. L.; Feng, Y. P.; Chen, W. Growth Intermediates for CVD Graphene on Cu(111): Carbon Clusters and Defective Graphene. *J. Am. Chem. Soc.* **2013**, *135*, 8409–8414.
  54. Wang, B.; Ma, X. F.; Caffio, M.; Schaub, R.; Li, W. X. Size-Selective Carbon Nanoclusters as Precursors to the Growth of Epitaxial Graphene. *Nano Lett.* **2011**, *11*, 424–430.
  55. Yuan, Q. H.; Gao, J. F.; Shu, H. B.; Zhao, J. J.; Chen, X. S.; Ding, F. Magic Carbon Clusters in the Chemical Vapor Deposition Growth of Graphene. *J. Am. Chem. Soc.* **2012**, *134*, 2970–2975.
  56. Kislov, V. V.; Mebel, A. M. The Formation of Naphthalene, Azulene, and Fulvalene from Cyclic C<sub>5</sub> Species in Combustion: An Ab Initio/RRKM Study of 9-H-Fulvalenyl (C<sub>5</sub>H<sub>5</sub>–C<sub>5</sub>H<sub>4</sub>) Radical Rearrangements. *J. Phys. Chem. A* **2007**, *111*, 9532–9543.
  57. Ferrari, A. C.; Meyer, J. C.; Scardaci, V.; Casiraghi, C.; Lazzeri, M.; Mauri, F.; Piscanec, S.; Jiang, D.; Novoselov, K. S.; Roth, S.; et al. Raman Spectrum of Graphene and Graphene Layers. *Phys. Rev. Lett.* **2006**, *97*, 187401.
  58. Luo, Z. T.; Kim, S.; Kawamoto, N.; Rappe, A. M.; Johnson, A. T. C. Growth Mechanism of Hexagonal-Shape Graphene Flakes with Zigzag Edges. *ACS Nano* **2011**, *5*, 9154–9160.
  59. Casiraghi, C.; Pisana, S.; Novoselov, K. S.; Geim, A. K.; Ferrari, A. C. Raman Fingerprint of Charged Impurities in Graphene. *Appl. Phys. Lett.* **2007**, *91*, 233108.
  60. Berciaud, S.; Ryu, S.; Brus, L. E.; Heinz, T. F. Probing the Intrinsic Properties of Exfoliated Graphene: Raman Spectroscopy of Free-Standing Monolayers. *Nano Lett.* **2009**, *9*, 346–352.
  61. He, R.; Zhao, L.; Petrone, N.; Kim, K. S.; Roth, M.; Hone, J.; Kim, P.; Pasupathy, A.; Pinczuk, A. Large Physisorption Strain in Chemical Vapor Deposition of Graphene on Copper Substrates. *Nano Lett.* **2012**, *12*, 2408–2413.
  62. Murdock, A. T.; Koos, A.; Ben Britton, T.; Houben, L.; Batten, T.; Zhang, T.; Wilkinson, A. J.; Dunin-Borkowski, R. E.; Lekka, C. E.; Grobert, N. Controlling the Orientation, Edge Geometry, and Thickness of Chemical Vapor Deposition Graphene. *ACS Nano* **2013**, *7*, 1351–1359.
  63. Zhao, L.; Rim, K. T.; Zhou, H.; He, R.; Heinz, T. F.; Pinczuk, A.; Flynn, G. W.; Pasupathy, A. N. Influence of Copper Crystal Surface on the Cvd Growth of Large Area Monolayer Graphene. *Solid State Commun.* **2011**, *151*, 509–513.
  64. Meca, E.; Lowengrub, J.; Kim, H.; Mattevi, C.; Shenoy, V. B. Epitaxial Graphene Growth and Shape Dynamics on Copper: Phase-Field Modeling and Experiments. *Nano Lett.* **2013**, *13*, 5692–5697.
  65. Jacobberger, R. M.; Arnold, M. S. Graphene Growth Dynamics on Epitaxial Copper Thin Films. *Chem. Mater.* **2013**, *25*, 871–877.
  66. Wofford, J. M.; Nie, S.; McCarty, K. F.; Bartelt, N. C.; Dubon, O. D. Graphene Islands on Cu Foils: The Interplay between Shape, Orientation, and Defects. *Nano Lett.* **2010**, *10*, 4890–4896.
  67. Giovannetti, G.; Khomyakov, P. A.; Brocks, G.; Karpan, V. M.; van den Brink, J.; Kelly, P. J. Doping Graphene with Metal Contacts. *Phys. Rev. Lett.* **2008**, *101*, 026803.



68. Khomyakov, P. A.; Giovannetti, G.; Rusu, P. C.; Brocks, G.; van den Brink, J.; Kelly, P. J. First-Principles Study of the Interaction and Charge Transfer between Graphene and Metals. *Phys. Rev. B* **2009**, *79*, 195425.
69. Gao, L.; Guest, J. R.; Guisinger, N. P. Epitaxial Graphene on Cu(111). *Nano Lett.* **2010**, *10*, 3512–3516.
70. Vanin, M.; Mortensen, J. J.; Kelkkanen, A. K.; Garcia-Lastra, J. M.; Thygesen, K. S.; Jacobsen, K. W. Graphene on Metals: A Van Der Waals Density Functional Study. *Phys. Rev. B* **2010**, *81*, 081408.
71. Cho, J.; Gao, L.; Tian, J.; Cao, H.; Wu, W.; Yu, Q.; Yitamben, E. N.; Fisher, B.; Guest, J. R.; Chen, Y. P.; *et al.* Atomic-Scale Investigation of Graphene Grown on Cu Foil and the Effects of Thermal Annealing. *ACS Nano* **2011**, *5*, 3607–3613.
72. Voloshina, E.; Dedkov, Y. Graphene on Metallic Surfaces: Problems and Perspectives. *Phys. Chem. Chem. Phys.* **2012**, *14*, 13502–13514.
73. Yoon, T.; Shin, W. C.; Kim, T. Y.; Mun, J. H.; Kim, T.-S.; Cho, B. J. Direct Measurement of Adhesion Energy of Monolayer Graphene as-Grown on Copper and Its Application to Renewable Transfer Process. *Nano Lett.* **2012**, *12*, 1448–1452.
74. Kisliuk, P. The Sticking Probabilities of Gases Chemisorbed on the Surfaces of Solids. *J. Phys. Chem. Solids* **1957**, *3*, 95–101.
75. Kolasinski, K. *Surface Science: Foundations of Catalysis Nanoscience*; Wiley: United Kingdom, 2012; p 574.
76. King, D. A.; Wells, M. G. Reaction-Mechanism in Chemisorption Kinetics - Nitrogen on (100) Plane of Tungsten. *Proc. R. Soc. London, Ser. A* **1974**, *339*, 245–269.
77. Luna, E.; Guzman, A.; Trampert, A.; Alvarez, G. Critical Role of Two-Dimensional Island-Mediated Growth on the Formation of Semiconductor Heterointerfaces. *Phys. Rev. Lett.* **2012**, *109*, 126101.
78. German, E. D.; Sheintuch, M. Predicting CH<sub>4</sub> Dissociation Kinetics on Metals: Trends, Sticking Coefficients, H Tunneling, and Kinetic Isotope Effect. *J. Phys. Chem. C* **2013**, *117*, 22811–22826.
79. Eden, M. In *Proceedings on the 4th Berkeley Symposium on Mathematical Statistics and Probability*; Neyman, F., Ed.; University of California Press: Los Angeles, CA, 1961; pp 223–239.
80. Becker, O. M.; Benshaul, A. Role and Mechanism of Island Formation in Chemisorption. *Phys. Rev. Lett.* **1988**, *61*, 2859–2862.
81. Artyukhov, V. I.; Liu, Y. Y.; Yakobson, B. I. Equilibrium at the Edge and Atomistic Mechanisms of Graphene Growth. *Proc. Natl. Acad. Sci. U.S.A.* **2012**, *109*, 15136–15140.
82. Whitesides, R.; Kollias, A. C.; Domin, D.; Lester, W. A.; Frenklach, M. Graphene Layer Growth: Collision of Migrating Five-Member Rings. *Proc. Combust. Inst.* **2007**, *31*, 539–546.
83. Treier, M.; Pignedoli, C. A.; Laino, T.; Rieger, R.; Mullen, K.; Passerone, D.; Fasel, R. Surface-Assisted Cyclodehydrogenation Provides a Synthetic Route Towards Easily Processable and Chemically Tailored Nanographenes. *Nat. Chem.* **2011**, *3*, 61–67.
84. Liu, T. H.; Gajewski, G.; Pao, C. W.; Chang, C. C. Structure, Energy, and Structural Transformations of Graphene Grain Boundaries from Atomistic Simulations. *Carbon* **2011**, *49*, 2306–2317.